11

Microminiature magnonic reservoir computer

© A.A. Nikitin,[1] R.V. Haponchyk,[1] I.Yu. Tatsenko,[1] M.P. Kostylev,[2] A.B. Ustinov[1]

[1]St. Petersburg Electrotechnical University „LETI"
197022 St. Petersburg, Russia
[2]University of Western Australia,
6009 Crawley, Western Australia, Australia
e-mail: aanikitin@etu.ru

Received May 22, 2024
Revised September 3, 2024
Accepted September 26, 2024

A model of a magnonic microreservoir based on a feedback loop with a nanometer-thick yttrium-iron-garnet film was developed. A simulation of the microreservoir response to an input electrical signal applied to an electronic attenuator from an arbitrary waveform generator was carried out. The microreservoirs of various designs were characterized with short-term memory and parity check tasks. Methods to increase the test capacities were considered. The maximum capacities of the short-term memory task of 5.02 and the parity check task of 1.29 were demonstrated. It was shown that the characteristics of the proposed magnonic microreservoirs are comparable with the magnonic reservoirs based on μm-thick yttrium-iron-garnet films.

Keywords: reservoir computers, magnonics, nonlinear spin waves, active ring resonator.

DOI: 10.61011/TP.2024.11.59753.190-24

Introduction

A considerable interest in artificial neural networks based on physical principles is currently observed. Reservoir computing systems (RCS) are a special case of such networks. Such systems have three layers of artificial neurons („nodes") — an input layer, a hidden layer with special properties and called „reservoir", and an output layer. The input layer is used to enter data into the reservoir, which is a large number of non-linearly interconnected nodes. The reservoir transforms a time-dependent stream of input data into a higher dimensional space in which the complex structures present in the input data become linearly separable [1,2]. The linear separation of the output data of the reservoir is performed by the output layer. This allows training only the output layer of the RCS and provides an important advantage of such systems in versatility and learning speed. A number of mechanical [3], optoelectronic [4,5], optical [6,7], memristor [8,9], spintronic [10,11] and other systems [12–16] have been recently proposed that can be successfully used for the physical implementation of reservoir computing. Performance, processing speed, memory capacity, energy efficiency and the size of the physical system are the main characteristics of physical reservoirs. The performance and memory capacity of different systems can be compared by using specially designed benchmark tests which allow evaluating both the fading memory (short-term memory test (STMT)) and the possibility of nonlinear data separation by a dynamic system (parity check test (PCT)). Such tests are unified, so they can be used to compare the performance of various RCS concepts [17–19].

A physical reservoir based on magnonic active ring oscillators (MARO) built on spin-wave delay lines (SWDL) with a feedback loop is one of the promising platforms [19–24]. It should be noted that due to the variety of dispersion properties of spin waves and their rich nonlinear dynamics, such ring systems are widely used to study various nonlinear effects and phenomena [25–35], and can also be used as magnonic co-processors [36,37]. The nonlinear dynamics of such oscillators ensures simultaneous computing and storage of information, which provides an advantage over other approaches which includes performance, learning speed, memory, energy efficiency and scalability [38], in addition, they can be used to build transmitters and sensors [39]. The SWDL design in such systems consists of two parallel microstrip antennas ensuring excitation and reception of spin waves, and an epitaxial film of yttrium iron garnet (YIG) magnetized to saturation with a thickness of the order of units of micrometers. The linear and nonlinear microwave properties of the SWDL determine the characteristics of the RCS, whose high performance is achieved with a distance between microstrip antennas of the order of units of millimeters [19–23]. Such sizes of the SWDL limit the possibility of microminiaturization of the RCS.

The microminiaturization of the structure is one of the tasks which need to be solved for the practical implementation of magnonic RCS. It is necessary to use ultrathin films with a thickness of hundreds or even tens of nanometers instead of films of micron thicknesses to solve this problem. This is attributable to the fact that the group velocity of spin waves decreases with the decrease of film thickness, which reduces the distance between the antennas from a few millimeters to several hundred or even tens of

micrometers, thus reducing the overall size of the device without compromising the introduced delay time.

The recent improvements in liquid-phase epitaxy technology made it possible to obtain IYG films of nanometer thickness grown on gadolinium gallium garnet (GGG) substrates, while maintaining excellent stoichiometry and crystal structure [38,40,41]. Currently, the liquid-phase epitaxy method can be used to obtain single-crystal YIG films with high uniformity from $\pm 8\%$ for films with a thickness of 30 nm and up to $\pm 0.8\%$ for films with a thickness of 100 nm. The diameter of the GGG substrates reaches 4 inches. At the same time, the magnetic dissipation parameter ΔH does not exceed 62 A/m at a frequency of 6.5 GHz. The use of nanometer-thick YIG films makes it possible to significantly reduce the size of SWDL and reservoirs based on them, which opens up prospects for the creation of microminiature spin-wave devices based on ultrathin YIG films.

Spin waves exhibit a wide variety of dispersion properties depending on the orientation of the external magnetic field and the direction of propagation. However, the configuration in which the spin waves excited by the antenna propagate in an in-plane magnetized film and perpendicular to the field direction is the most promising configuration from a practical point of view. This configuration ensures the propagation of surface spin waves (SSW), which in the case of nanometer-sized YIG films are characterized by extremely low group velocities, on the order of 100 m/s, and ensure a delay time τ sufficient for applications with a practically feasible distance between spin wave antennas.

The most effective spin-wave antennas for nanometer-thick films are antennas on coplanar transmission lines according to the analysis of the literature [42–51]. Such antennas are composed of three planar electrodes: a central signal electrode and two electrodes under the ground potential located at the edges. A self-consistent theory of excitation of spin waves in micron-thick YIG films by coplanar antennas with edge electrodes unlimited in width was developed in Ref. [43,46,47]. An improved self-consistent theory was proposed in the theoretical study [50]. This theory describes the process of excitation, propagation and reception of spin waves in ultrathin magnetic films by coplanar antennas, which have an arbitrary width of the edge electrodes and a finite value of the electrical resistivity of the metal electrodes of the antenna. It should be noted that the problem of reception of spin waves by a coplanar antenna is solved separately in Ref. [50]. This feature makes it possible to separate the process of excitation of spin waves from their reception, which is important for describing the nonlinear propagation of spin waves in ferromagnetic films. This theory is in good agreement with the results of the study presented in Ref. [51] which experimentally showed a strong decoupling of coplanar antennas and demonstrated their additional advantage associated with a shift in the maximum excitation efficiency to the region of relatively large wave numbers. The range of operating wave numbers excited by the antenna is determined by its geometry in this case. This feature makes it possible to ensure effective excitation of spin waves in a narrow range of wave numbers, which, in accordance with the law of dispersion of spin waves, determines the operating frequency band, which ultimately allows the creation of narrow-band spin-wave transmission lines.

The theoretical model developed in Ref. [50] was used to model the performance characteristics of a microminiature MARO containing SWDL on nanometer YIG films in the feedback loop [52]. As a result, it was shown that the proposed design ensures a phase noise level of -115 dB/Hz at 10 kHz offset from the oscillation frequency of 5 GHz with a film thickness of 100 nm and a distance between coplanar antennas of 56 μm. The use of such a MARO design makes it possible to significantly reduce the size of the RCS. However, the characteristics of the RCS on nanometer-sized YIG films have not been studied to date. The purpose of this paper is a theoretical study of the effect of the parameters of the SWDL on nanometer YIG films on the characteristics and performance of a microminiature reservoir computing system. A theoretical model describing the transient processes in MARO will be used for this purpose [53]. Such a model can be used not only to describe the results observed in the experiment, but also to predict the characteristics of the reservoir computing system [54].

1. Impact of the parameters of a microminiature spin-wave delay line on its transmission characteristics

A three-stage numerical calculation procedure was developed to simulate transient processes in a microminiature MARO. The complex transmission coefficient of a miniature SWDL was modeled at the first step using the theoretical model described in Ref. [50], which is schematically shown in Fig. 1. The explanation of the symbols shown in the figure is given below: l_d — distance between the centers of symmetry of the coplanar antennas (length of the SWDL); l_s — length of the coplanar antennas; H — external magnetic field; w_g — width of the edge grounded electrodes, w — width of the central electrode; Δ_g — width of the gaps between the edge and central electrodes.

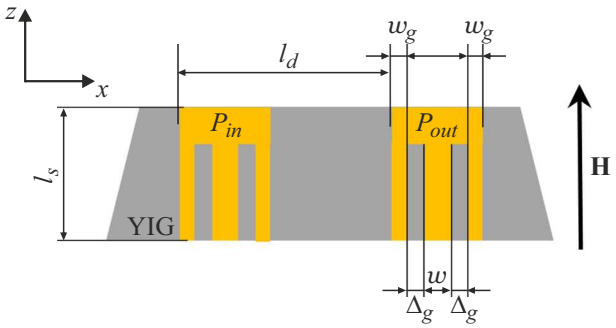

Figure 1. Scheme of the SWDL with coplanar antennas.

Fig. 1 shows that the studied design has many parameters, which determines the microwave properties of the studied SWDL. We will consider the impact of various parameters relative to the basic design of the delay line to simplify the analysis task. Typical values of the thickness of the YIG film of $L = 100\,\text{nm}$, the Hilbert attenuation coefficient $\alpha = 1 \cdot 10^{-4}$ and saturation magnetization $M_s = 139.26\,\text{kA/m}$, as well as the magnetic field strength $H = 85.94\,\text{kA/m}$ are chosen as basic parameters. Such parameters ensure the frequency of homogeneous ferromagnetic resonance in an unbounded in the plane tangentially magnetized YIG film $f_\perp = \mu_0 \frac{|\gamma|}{2\pi}\sqrt{H(H+M_s)} = 4.9\,\text{GHz}$, where $|\gamma| = 1.761 \cdot 10^{11}\,\text{rad}/(\text{s}\cdot\text{T})$ — gyromagnetic ratio, and $\mu_0 = 4\pi \cdot 10^{-7}\,\text{H/m}$. The resistivity of the metal electrodes of the antennas is $\rho = 2.65 \cdot 10^{-8}\,\Omega\cdot\text{m}$. The parameters of the coplanar antennas of the basic design are chosen in such a way as to ensure effective excitation of surface spin waves in the YIG film in case of a change of the geometric parameters of the antenna. The effective excitation means such an excitation in which the minimum value of the reflection coefficient modulus $|\Gamma|_{\min}$ in the operating frequency range is less than 0.5 (voltage standing-wave ratio (VSWR) is less than 3). The geometric parameters of the antennas of the basic design $w = 650\,\text{nm}$, $w_g = 325\,\text{nm}$, $\Delta_g = 335\,\text{nm}$, $l_s = 20\,\mu\text{m}$ ensure $|\Gamma|_{\min} = 0.433$ (VSWR = 2.53). This paper further studies the impact of the following parameters: L, w, w_g, Δ_g, l_s, H and ρ on the transmission coefficients of the SWDL and ring resonator built on it, as well as on the performance of the magnonic RCS. The above parameters determine the shape of the transmission coefficient (the position of the frequency of the maximum transmission coefficient, the operating frequency band). During modeling the geometric parameters change to $\pm 30\%$ relative to the basic design. Such a change, on the one hand, allows preserving the micron dimensions of the antennas, and on the other hand, determining the parameters that have the strongest impact. Values close to the limit (for the magnetic field) or ideal (for the conductivity of the electrodes) were used to demonstrate the effect of the magnetic field strength and the conductivity of the electrodes.

The exciting coplanar antenna converts the input microwave signal into a SSW, which propagates in the film along the x axis. The receiving coplanar antenna has the same geometry and is located at a distance of $l_d = 20\,\mu\text{m}$ from the input antenna. It converts the SSW back into a microwave signal coming to the output of the delay line. It should be noted that the distance between the antennas l_d does not affect the shape of the transfer characteristic unlike the above parameters. The value l_d is chosen in such a way that the minimum delay time of the signal in the ring at the frequency corresponding to the position of the maximum transmission coefficient (minimum reflectance $|\Gamma|_{\min}$) for all studied structures is at least 70 ns with an insertion loss level of no more than 35 dB. This is attributable to the need to compensate for the losses introduced by the SWDL using a microwave amplifier to switch the circuit to auto-oscillation mode.

The theoretical model was used to calculate the complex transmission coefficient of the SWDL shown in Fig. 1 [50]. The calculation result for this model can be written as follows:

$$\mathbf{T_{sw}} = |T_{sw}| \exp(i\Phi_{sw}), \tag{1}$$

where $S_{21} = |T_{sw}|^2$ and Φ_{sw} describe the amplitude-frequency and phase-frequency characteristics of the studied SWDL, respectively.

Figs. 2 and 3 show the results of calculation of the amplitude-frequency and phase-frequency characteristics of SWDL of various designs, in which one of the parameters differs from the base case. The transmission characteristic of the SWDL of the basic design is shown for comparison with a solid black line in these figures. Fig. 2, *a, b* shows that an increase of the widths of the edge electrodes (w_g) and the gap between the central and edge electrodes (Δ_g) results in a slight change of the transmission characteristic, namely, a shift in the maximum position down in frequency, as well as a reduction of the level of insertion loss. However, the increase of the width of the central electrode to $w = 885\,\text{nm}$ (Fig. 2, *c*) leads to a significant increase of bandwidth and an increase of losses. On the other hand, the reduction of the electrode width has little effect on the shape of the transmission characteristic. The increase of the antenna length to $l_s = 35\,\mu\text{m}$ (Fig. 2, *d*) allows for a significant reduction of the level of insertion losses, which is associated with an increase of the active resistance of the antennas. As a result, the input impedance of the antennas approaches $Z_0 = 50\,\Omega$ and the reflectance decreases. A further increase of length to $l_s = 50\,\mu\text{m}$ has little effect on the transmission characteristics, which is primarily associated with an increase of attenuation introduced by the active (ohmic) resistance of the antennas. The effect of the active resistance of antennas is demonstrated in Fig. 2, *e* by showing the results of calculating the transmission characteristic in the case of ideal electrodes at $\rho \to 0$ (the resistivity value was chosen in the calculation to be different from zero, but was significantly less than the base case). As can be seen in this figure, the width of the transmission characteristic and the insertion loss significantly increase. This behavior is due to the fact that a decrease of the resistivity of the electrodes results in a decrease of their active resistance, as a result of which the antenna exhibits a significantly lower input impedance and, consequently, a higher reflectance. For example, for the case shown in Fig. 2, *e*, at the frequency corresponding to the position of the maximum transmission characteristic, the antenna at $\rho \to 0$ has an input impedance $Z_{in} = 1.73 + j \cdot 0.94\,\Omega$, which corresponds to the value of the reflection coefficient $|\Gamma|^2 = 0.87$. At the same time, for the base case, the input impedance is $Z_{in} = 19.77 + j \cdot 0.94\,\Omega$, which corresponds to $|\Gamma|^2 = 0.19$. It should be noted that ohmic losses will dominate over other attenuation mechanisms with a significant increase of the resistivity of the antennas. The

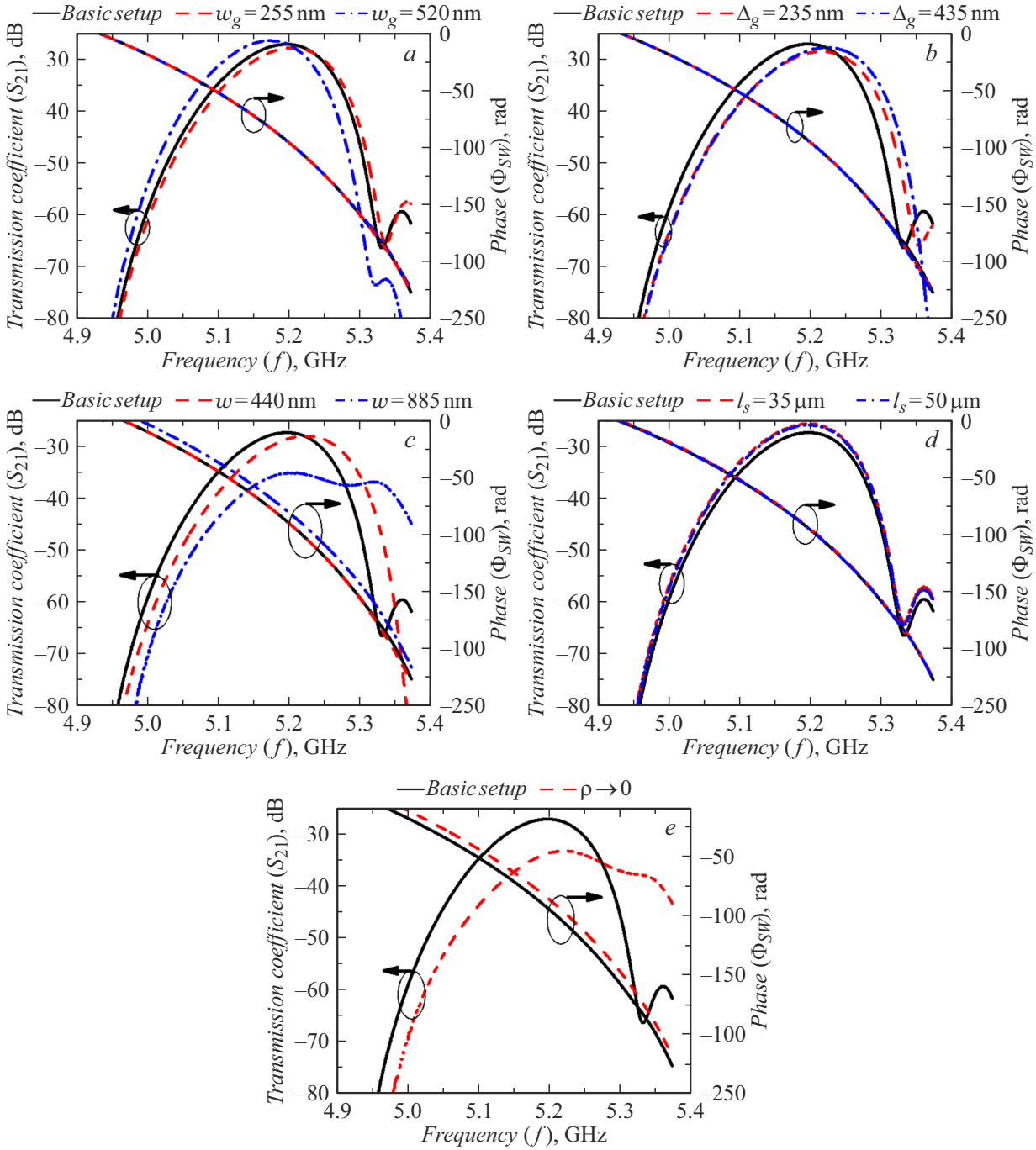

Figure 2. Impact of the width of the edge electrodes (w_g) (a); width of the gap between the central and edge electrodes (Δ_g) (b); width of the central electrode (w) (c); antenna lengths (l_s) (d); conductivity of the electrodes of the coplanar antenna (ρ) (e) on the SWDL transmission characteristics.

obtained results allow concluding that the resistivity and length of the antennas should be selected consistently. From the characteristics shown in Fig.2, it can be seen that coplanar antennas place high demands on manufacturing technology.

It should be noted that changing the antenna parameters does not affect the dispersion properties of the wave propagating in the delay line, therefore the phase-frequency characteristics in Fig. 2, *a, b, d* coincide. The shift of the phase-frequency characteristics in Fig. 2, *c, e* is attributable to the upward shift of the operating frequency band. However, the dependence of the delay time on the frequency $\tau(f) = d\varphi(f)/d\omega$ does not change in both cases.

Let us now consider the impact of the thickness of the YIG film (Fig. 3, *a*) and the magnitude of the magnetic field (Fig. 3, *b*). As can be seen from the figures, a decrease

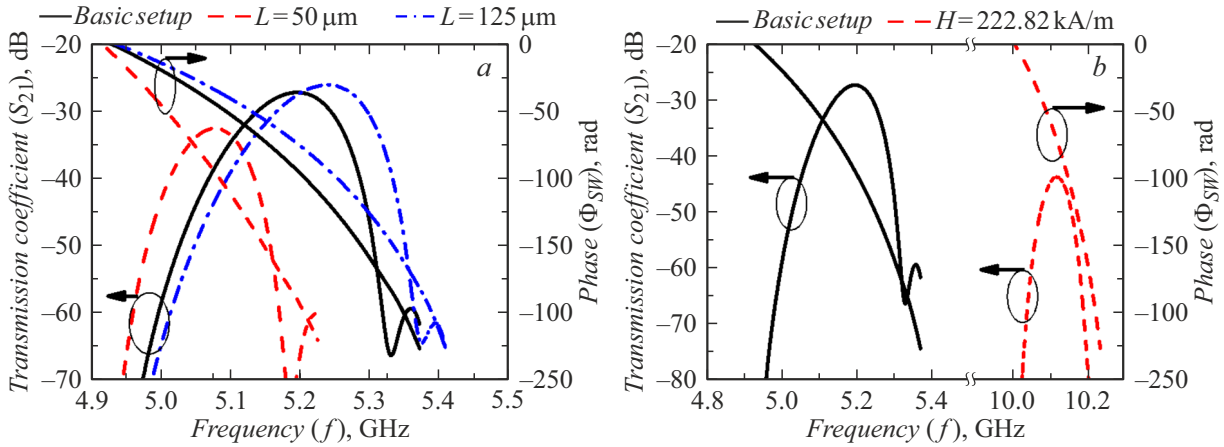

Figure 3. Impact of the thickness of the YIG film (L) (a); the magnitude of the magnetic field (H) (b) on the SWDL transmission characteristics

of film thickness and an increase of the magnetic field ensures an increase of attenuation and significantly narrows the width of the operating frequency band. This behavior is attributable to a decrease of the group velocity of spin waves. It should be noted that an increase of the magnetic field results not only in a decrease of the group velocity, but also in an upward frequency shift of the spectrum of operating spin waves. In both cases, a decrease of the group velocity leads to an increase of the steepness of the phase-frequency characteristics.

The results presented in this part of the work show that a feature of coplanar antennas is the strong suppression of the microwave signal outside the SWDL bandwidth. This is a key feature for designing of ring resonators, auto-oscillators and magnonic RCS. Strong decoupling is necessary to prevent the transition of ring circuits to auto-oscillation mode at frequencies located outside the spectrum of operating spin waves.

2. Impact of the parameters of a microminiature SWDL on the transmission characteristics of an active ring resonator based on it

The second step is to simulate the transmission characteristic of the MARO, which includes a SWDL, as well as compact microelectronic elements such as directional couplers for signal input and output, a microwave amplifier and an attenuator to control the amplitude of the signal circulating in the ring (Fig. 4). Such a system is a magnonic active ring resonator (MARR) up to the threshold of auto-oscillation.

An original theory based on the partial wave method was used to calculate the transmission characteristics of the MARR [55]. To take into account the features of excitation, propagation and reception of spin waves in delay lines on nanometer films of YIG with coplanar antennas, the

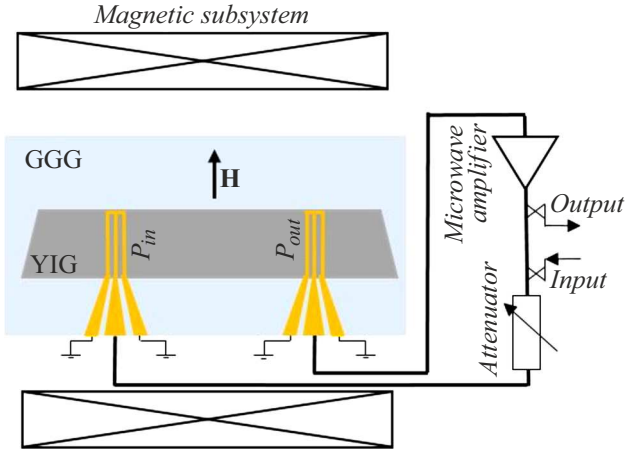

Figure 4. MARR circuit on a microminiature SWDL.

formula for calculating the power transmission coefficient was written as

$$H_p = \kappa_1\kappa_2|T_{sw}|^2G^2 \,/\, \left[(1-\kappa_1)(1-\kappa_2)|T_{sw}|^2G^2 - 2\sqrt{1-\kappa_1}\sqrt{1-\kappa_2}|T_{sw}|G\cos(\Phi_{sw}) + 1\right], \quad (2)$$

where κ_1 and κ_2 — coupling coefficients of directional couplers used for microwave signal input and output, respectively; $G = G_0 \cdot A$ — effective gain, and G_0 and A — the gain coefficients of the microwave amplifier and attenuation introduced by the attenuator, in amplitude, respectively. It should be noted that we consider the phase shift accumulated in the electronic circuits of the ring to be negligible in the expression (2) compared to the phase shift accumulated in the SWDL, which makes it possible to neglect the delay time in these circuits.

The amplitude-frequency characteristics of the SWDL of various designs studied in the previous part of the work is shown by black dotted lines in Fig. 5–11. The transmission characteristic of the MARR on the SWDL of the basic

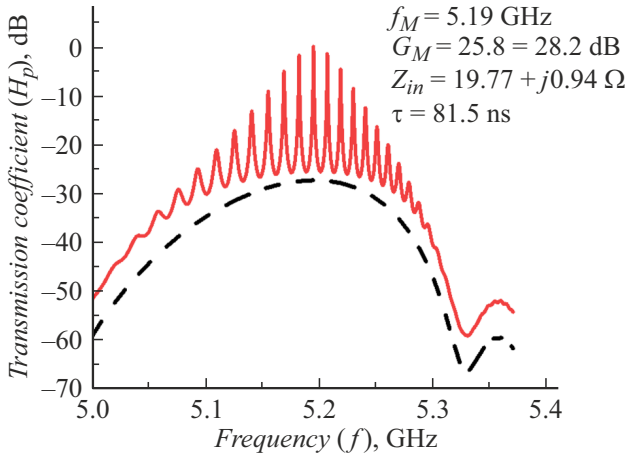

Figure 5. Amplitude-frequency characteristics of both the MARR (solid line) and the microminiature SWDL of the basic design (dashed line).

structure is shown by the solid line in Fig. 5, and results of calculation for the remaining SWDL structures are shown by solid line in Fig. 6–11. The value of the parameter, which differs from that used in the basic design of the SWDL, is shown in the upper right corner of the figures. The expression (2) was used to model the transmission characteristics of the MARR. Here and further, the coupling coefficients $\kappa_1 = \kappa_2 = 0.1$ are used for calculations, which correspond to common practically used 10 dB directional couplers.

Fig. 5 shows that the transmission characteristics of the ring resonator on the SWDL of the basic design demonstrate a multi-frequency resonant response. Each of the peaks corresponds to a discrete resonant harmonic of the ring. The position of the resonant frequencies is determined by the phase condition under which the phase shift accumulated in the SWDL Φ_{sw} is a multiple of 2π. The transmission coefficient of the ring at the resonant frequency and the quality factor of the resonant harmonics is determined by the ratio between the signal loss per single round trip over the ring and the magnitude of the amplifier gain in the feedback loop. An increase of the gain results in an increase of the transmission coefficient and the quality factor of the resonant harmonics [56,57]. As can be seen from Fig. 5, one of the harmonics with a frequency of f_M stands out relative to the others. This harmonic is characterized by the lowest losses introduced by the SWDL, therefore, the amplitude of the signal circulating in the ring at this frequency is maximum. Let us denote such a transfer coefficient $|T_{sw}|_M$. For ease of comparison, all the results of calculations of the MARR transmission characteristics are given for such an effective gain G_u, at which $H_p(f_M) = 1$ (or $H_p(f_M) = 0$ dB). The value of the gain required to fulfill this condition is obtained from the expression (2) and we write it in the following form:

$$G_u = \frac{1}{\left(\sqrt{1-\kappa_1}\sqrt{1-\kappa_2} + \sqrt{\kappa_1\kappa_2}\right)|T_{sw}|_M}. \quad (3)$$

A further increase of the gain will be accompanied by an increase of the amplitude of the output signal. As soon as the losses are fully compensated, the ring will switch to the auto-oscillation mode of the monochromatic signal at a frequency of f_M [52]. This condition is fulfilled when the denominator of the expression (2) is zeroed. Then the gain factor, which ensures the transition of the ring to the auto-oscillation mode, will be written as follows:

$$G_M = \frac{1}{\sqrt{1-\kappa_1}\sqrt{1-\kappa_2}|T_{sw}|_M}. \quad (4)$$

For clarity, Figure 5–11 in the upper right corner shows information about the value of the auto-oscillation threshold G_M, the input impedance of coplanar antennas Z_{in}, as well as the signal delay time τ at a frequency of f_M. Determining a set of parameters that ensure the maximum delay time τ with a minimum auto-oscillation threshold G_M is the most interesting task from the point of view of the characteristics of the reservoir computing system.

Fig. 6–9 show the impact of antenna parameters on the transmission characteristics of MARR built on microminiature SWDL. The change of w_g and Δ_g has a similar effect as shown earlier. The increase of the width of the edge electrodes (w_g) (Fig. 6, *a, b*) and the gap between the central and edge electrodes (Δ_g) (Fig. 6, *c, d*) leads to a slight downward frequency shift of the maximum position, as well as a decrease of the level of insertion losses. As a result of this shift, compared with the basic design (Fig. 5), the auto-oscillation threshold G_M decreases, and the delay time of spin waves at the frequency f_M decreases by 7 ns for the case presented in Fig. 6, *b*, and by 5 ns for Fig. 6, *d*. It should be noted that an increase of Δ_g also results in an increase of the impedance resistance to $Z_{in} = 19.98 + j0.69\ \Omega$ and, therefore, this design ensures a lower auto-oscillation threshold $G_M = 27.25$ dB (Fig. 6, *d*).

Let us now consider the effect of the width of the central electrode (w). As can be seen from Fig. 7, *a*, the reduction of the width of the central electrode to $w = 440$ nm results in a upward frequency shift of the maximum of transmission coefficient. As a result, the delay time increases by 5 ns. In this case, an increase of the input resistance to $Z_{in} = 24.16 + j1.36\ \Omega$ partially compensates for the increase of spin wave attenuation. As a result, the auto-oscillation threshold is $G_M = 29$ dB. An increase of the width of the electrode (Fig. 7, *b*) results in a broadening of the transmission characteristic and additional attenuation. As a result, the auto-oscillation threshold significantly increases, and the delay time practically does not change.

Fig. 8 shows the results of calculation of the transmission characteristics of active ring microresonators on the SWDL containing antennas of various lengths (l_s). As noted earlier,

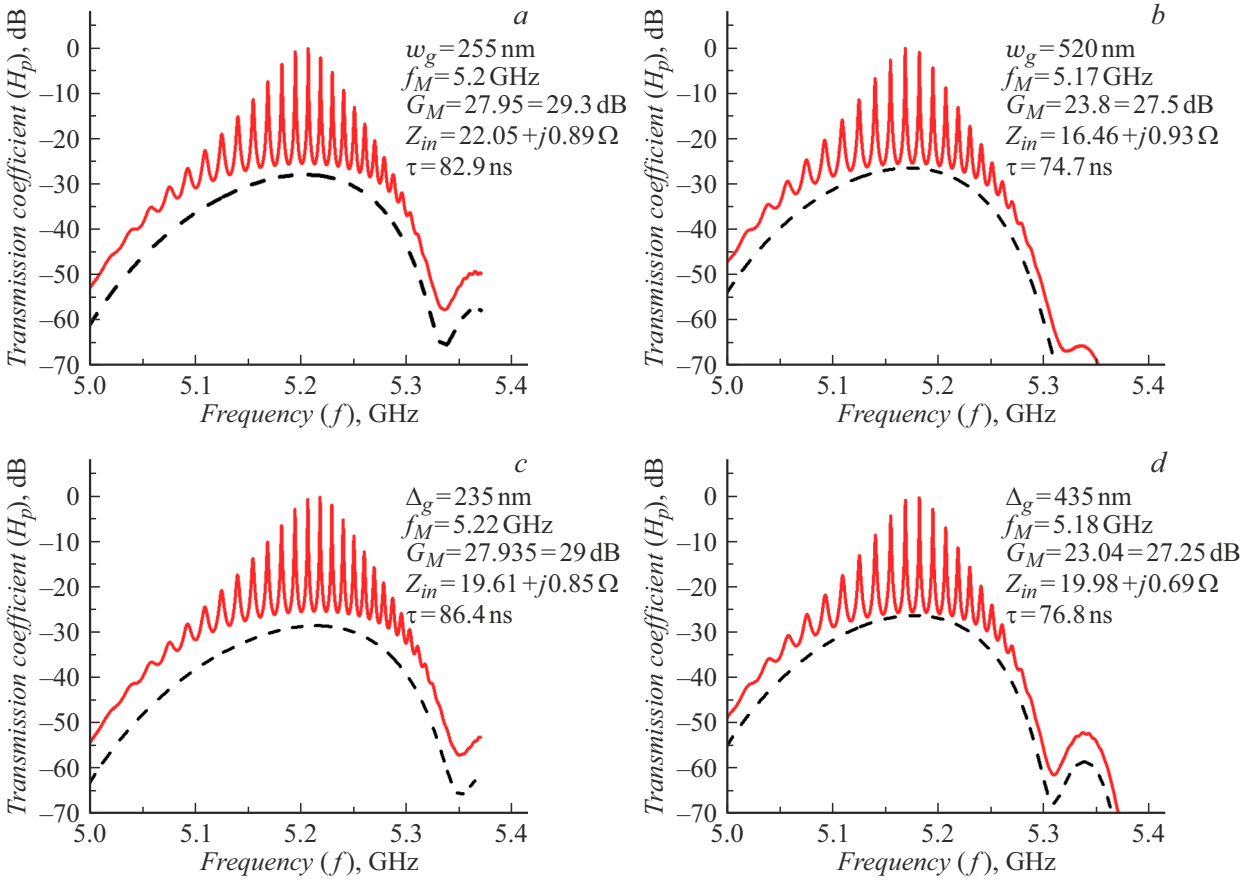

Figure 6. Amplitude-frequency characteristics of the MARR (red solid line) and microminiature SWDL (black dashed line), calculated at $w_g = 255$ nm (a); $w_g = 520$ nm (b); $\Delta_g = 235$ nm (c); $\Delta_g = 435$ nm (d).

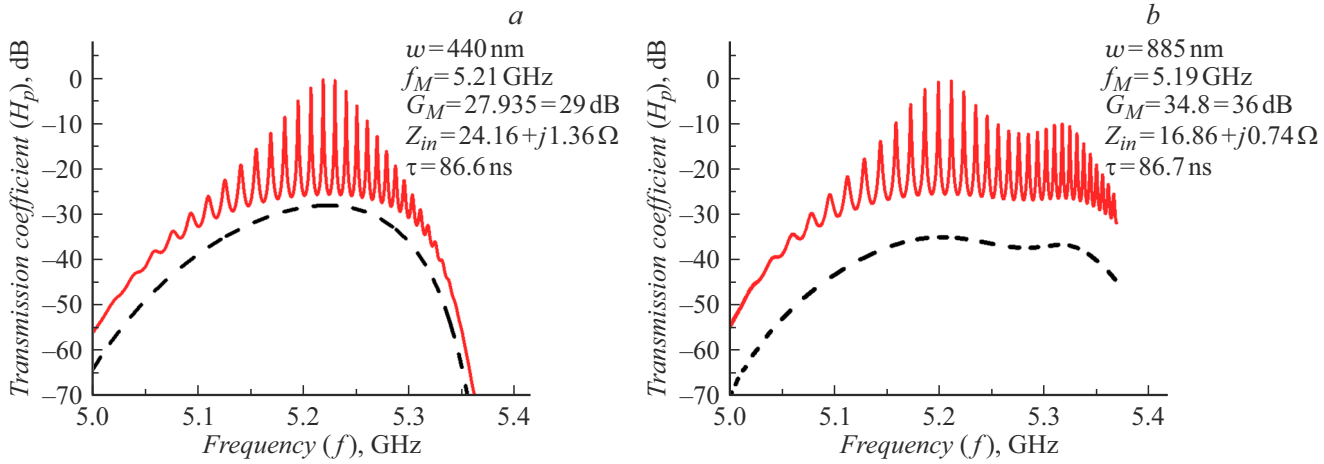

Figure 7. Amplitude-frequency characteristics of the MARR (red solid line) and microminiature SWDL (black dashed line), calculated at w, nm: 440 (a); 885 (b).

the increase of the length of the antenna results in an increase of the input impedance. The input impedance of the antenna with length of $l_s = 50\,\mu$m is $Z_{in} = 49.5 + j2\,\Omega$ at frequency f_M. As a result, this design ensures the longest delay time of $\tau = 86.6$ ns with the lowest threshold gain of $G_M = 26.5$ dB. It should be noted that the results obtained for an antenna with a length of $l_s = 50\,\mu$m are close to the results for an antenna with a length of $l_s = 35\,\mu$m (Fig. 8, b). This is attributable to an increase of the active resistance of long antennas, which, despite a decrease of the reflection coefficient, introduce additional losses into the propagation of the signal. We use a well-known expression

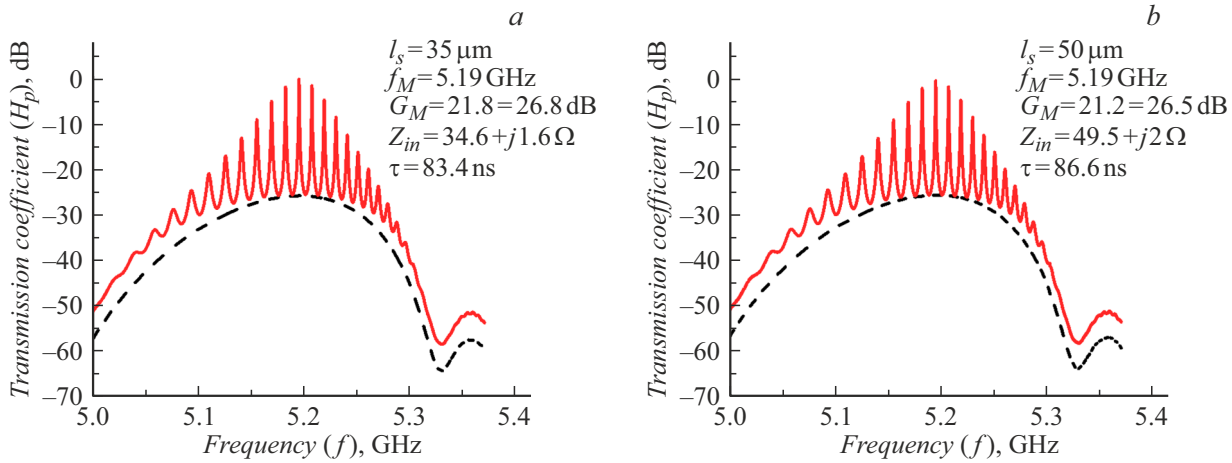

Figure 8. Amplitude-frequency characteristics of the MARR (red solid line) and microminiature SWDL (black dashed line), calculated at l_s, μm: 35 (*a*); 50 (*b*).

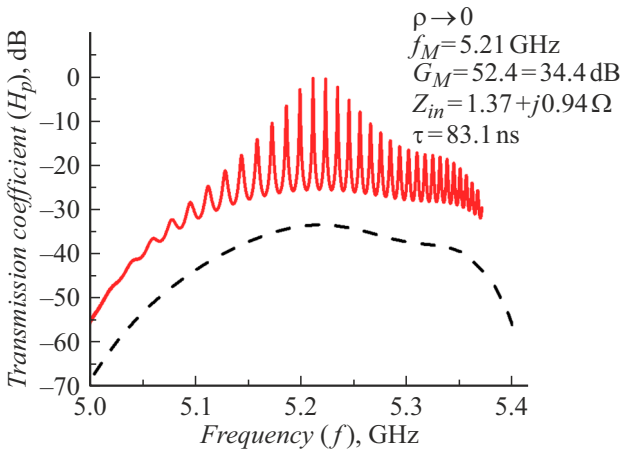

Figure 9. Amplitude-frequency characteristics of the MARR (red solid line) and microminiature SWDL (black dashed line), calculated with $\rho \to 0$.

relating the attenuation of spin waves A, expressed in dB, and delay time τ in microseconds to compare the delay time $\tau = 86.6$ ns obtained in Fig. 8, *b* at $G_M = 26.5$ dB with the characteristics typical for SWDL on films of micron thickness:

$$A(\text{dB}) \approx 0.95 \cdot 2\Delta H \cdot \tau\ [\mu\text{s}]. \qquad (5)$$

Hence we obtain $A = 10$ dB with a delay time of $\tau = 86.6$ ns. However, such a delay time in the case of a micron-thick YIG film requires a distance between the antennas of the order of several millimeters.

Another important parameter of coplanar antennas is the resistivity of the electrodes (ρ). Figure 9 shows the results of calculation of the transmission characteristic of an active ring resonator for the case of ideal electrodes at $\rho \to 0$. As noted above, ideal antennas ensure a low input impedance $Z_{in} = 1.37 + j0.94\,\Omega$, as a result of which the threshold for switching to auto-oscillation mode of such an annular microresonator increases to 34.4 dB.

Let's consider the impact of the magnetic film parameters. Figure 10 shows the results of calculation of the transmission characteristics of active ring resonators for YIG films of different thicknesses. A change of the YIG film thickness is known to affect the delay time and the level of insertion losses. An increase of thickness to $L = 125$ nm results in a decrease of the delay time by 3.8 ns, while the oscillation threshold decreases by 1 dB (Fig. 10, *a*). On the other hand, the reduction of the thickness to $L = 50$ nm leads to an increase of the delay time by 20.9 ns, as well as an increase of the auto-oscillation threshold by 5.4 dB as shown in Fig. 10, *b*. As can be seen from this figure, a significant increase of the delay time is accompanied by a decrease of the distance between adjacent resonant frequencies. Thus, the distance between adjacent frequencies near the frequency f_M for the basic design is 12.1 MHz, and in the case of a thin film of a YIG, this distance is reduced to 8.8 MHz.

Figure 11 shows the transmission characteristic of an active ring microresonator calculated for the magnetic field of $H = 222.82$ kA/m. As can be seen, the delay time increases by 49.6 ns as a result of the magnetic field increase, which is accompanied by an increase of the auto-oscillation threshold by 16.5 dB, as well as a decrease of the distance between neighboring resonant frequencies by 4.7 MHz.

3. Theoretical study of the performance of magnonic RCS on microminiature SWDL

The increase of the gain above the threshold (G_M) puts the active ring resonator into monochromatic auto-oscillation mode at a frequency of f_M. The output power in this mode is determined by the balance between the gain given by the microwave amplifier in the feedback loop and the nonlinear

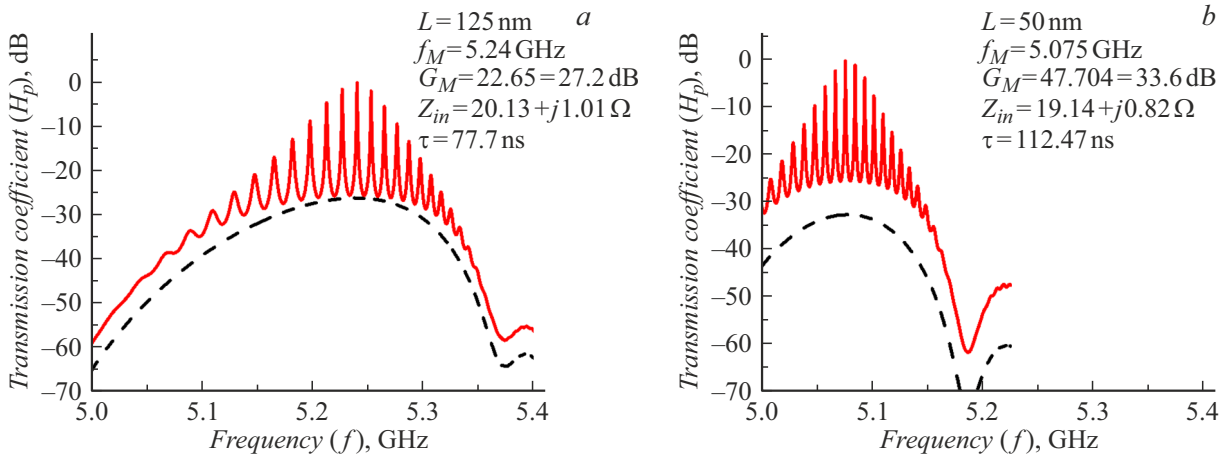

Figure 10. Amplitude-frequency characteristics of the MARR (red solid line) and microminiature SWDL (black dashed line), calculated with L, nm: 125 (a); 50 (b).

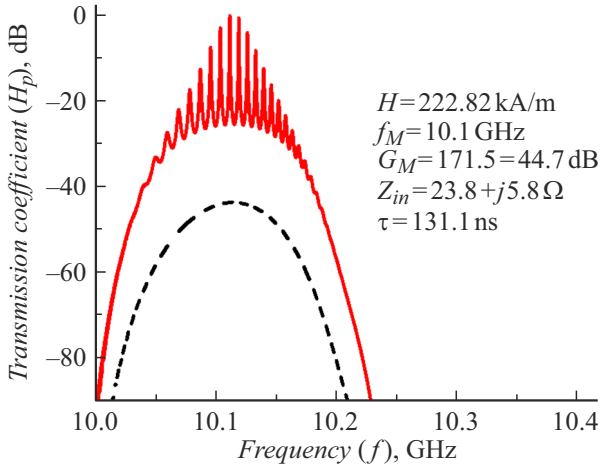

Figure 11. Amplitude-frequency characteristics of the MARR (solid line) and microminiature SWDL (dashed line), calculated with H = 222.82 kA/m.

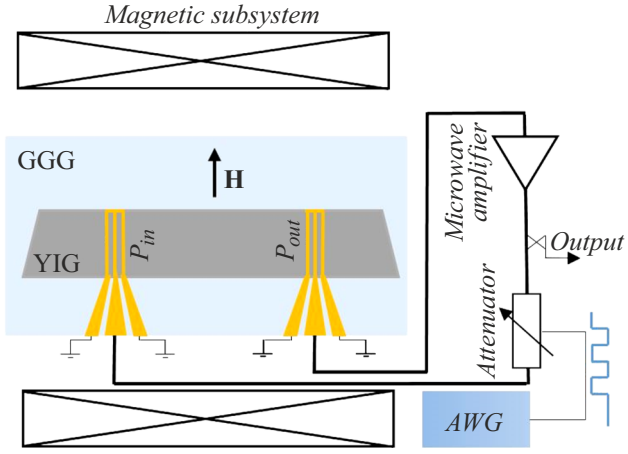

Figure 12. Circuit of a magnonic reservoir computing system based on a microminiature SWDL.

damping of spin waves in the SWDL. Any change of the gain leads to a disruption of this balance which results in the variation of the output signal power until the balance between gain and damping is restored. The transients occurring at the MARO output in case of the gain change allow such a circuit to be used as a RCS [19–22].

The block diagram of the RCS on the microminiature SWDL is shown in Fig. 12. Unlike the MARR circuit shown in Fig.4, the RCS contains one directional coupler that ensures the output of a microwave signal from the ring, as well as an electronic attenuator (modulator) used to inject an information sequence from an arbitrary waveform generator (AWG) by controlling the gain in the feedback loop.

The MARO response to a random input sequence of pulses applied to the input to the electronic attenuator was simulated at the final stage. The calculations are performed using a numerical model based on the Landau–Ginzburg Equation for fourier components describing the nonlinear phase shift and nonlinear damping of spin waves propagating along the axis x [34,58,59]:

$$V_g\left(\frac{\partial u}{\partial x}+i\frac{\partial \varphi_{NL}}{\partial x}u\right)+\eta u+(\upsilon_1+iN)u^3+\upsilon_2 u^5=0, \quad (6)$$

where $u=\frac{m}{\sqrt{2}M_s}$ — dimensionless amplitude of the spin wave, m — variable component of magnetization, φ_{NL} — nonlinear phase shift, $V_g=\frac{\partial\omega}{\partial k}$ — group velocity of spin wave, $N=\frac{\partial\omega}{\partial|u|^2}$ — nonlinear coefficient, $\eta=\mu_0\cdot|\gamma|\cdot\Delta H$ — relaxation frequency of spin waves, υ_1 and υ_2 — cubic and quintic nonlinear damping parameters, respectively. The equating of the real and imaginary parts of the equation (6) to zero yields two differential equations that describe the evolution of the amplitude and phase of a nonlinear spin wave. Further, the transients in the RCS are

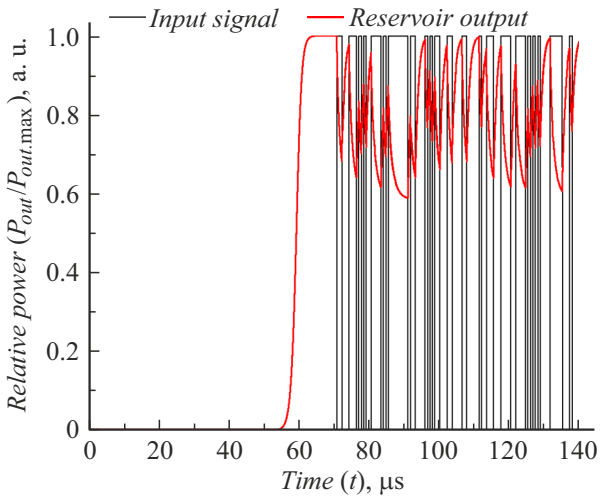

Figure 13. Response of the MARO (red line) to the input binary sequence (black line).

described by using only the equation for the amplitude:

$$\frac{\partial u}{\partial x} + \frac{\upsilon_1}{V_g}u^3 + \frac{\upsilon_2}{V_g}u^5 + \frac{\eta}{V_g}u = 0. \qquad (7)$$

Solving the equation (7) allows determining the amplitude of the signal at the output of the nonlinear SWDL [58]. In accordance with the scheme shown in Fig.12, the signal received at the output of the SWDL propagates through the electronic components of the ring, including an amplifier ensuring the loss compensation ($G > G_M$). Part of the signal is output from the ring, and the remaining part of the signal is transmitted at the input of the SWDL and is used as the initial amplitude for solving the equation (7). Repeating this calculation at each signal round trip over the ring allows describing the transient processes that occur in the MARO in case of the change of the gain in the feedback loop [53]. The method proposed in this work was used to simulate the RCS response, which is the dependence of the power of the MARO output signal on time.

Fig. 13 shows the RCS response (red line) to the input binary sequence shown by the black line. The parameters of the SWDL of the basic design were used for modeling, as well as the following values of the cubic $\upsilon_1 = 2\,\text{ns}^{-1}$ and quintic $\upsilon_2 = 2\,\text{ps}^{-1}$ nonlinear damping parameters. It should be noted that the ratio of the input pulse duration T to the signal delay time in the SWDL $\tau(T/\tau)$ is one of the key parameters determining the performance characteristics of the RCS. In this case, the duration of the transient process between two stable states is determined by the ratio between the gain coefficient and damping parameters of spin waves. The lower gain value is limited by the auto-oscillation threshold in RCS based on MARO, and the upper gain value is limited by the threshold of occurrence of nonlinear effects of a higher order. As shown in the Ref. [22,60], such RCS on micron films of YIG demonstrate high performance at T/τ from 5 to 10. The delay time varied from 74.7 to 131.1 ns in the studied microminiature SWDL. Therefore, the single pulse duration in the binary sequence was chosen to be equal to $T = 700$ ns, which corresponds to T/τ range from 5.34 to 9.37.

An information signal is sent from the AWG to the input to the electronic attenuator. The attenuator does not introduce losses when the logical „0“ is applied, i.e. the effective gain in the ring (transmission coefficient of the amplifier and electronic attenuator) is $G_{on} = \sqrt{1.1}G_M = G_M + 0.4\,\text{dB}$. The attenuator reduces the effective gain to $G_{off} = \sqrt{1.05}G_M = G_M + 0.2\,\text{dB}$ when the logical „1“ is applied. The input binary sequence consisted of 200 bits in the calculation. The first 100 values are „0“. They are necessary to put the ring into auto-oscillation mode. The remaining 100 bits are randomly generated.

The ring enters auto-oscillation mode after 60 μs (red line) as can be seen in Fig. 13. An arbitrary sequence is applied to the input of the electronic attenuator after 70 μs ensuring the change of the gain factor and resulting in the transients at the MARO output (red line in Fig. 13).

The calculation of the capacities of the parity test and the short-term memory test is one of the methods for evaluating the RCS performance. A binary sequence with a length of 4200 bit was applied to the input to the magnonic micro-reservoir for this purpose. The first 200 bits in this sequence had the value „0“, the remaining 4000 bits were filled with a random binary sequence. Figure 14 shows the results of calculating the capacities of the STMT and PCT for micro-reserves on the SWDL of the basic design. The figure shows that the values of the STMT and PCT capacities reach 3.99 and 0.59, respectively, in this case.

The STMT and PCT capacities obtained for magnonic RCS on SWDL of various designs studied in this paper are summarized in the table. The parameter of the SWDL is provided in the table in the second column the value of which differs from the basic design. The third and fifth columns correspond to STMT and PCT capacities. The fourth and sixth columns correspond to a change of capacity compared to the capacity of the tests for the SWDL of the basic design. The ratio of the pulse duration T to the SWDL delay time τ is provided in the rightmost column.

As can be seen from the table, the obtained capacitance values indicate that the selected parameters of the basic design and the selected delay time are not optimal. The maximum PCT value was obtained with the ratio $T/\tau = 9.11$. One of the ways to increase the STMT and PCT capacities is to choose the optimal ratio between the delay time in the ring and/or the duration of the input pulses. The results obtained in the study demonstrate the fundamental applicability of microminiature SWDLs for the creation of magnonic micro-reservoirs.

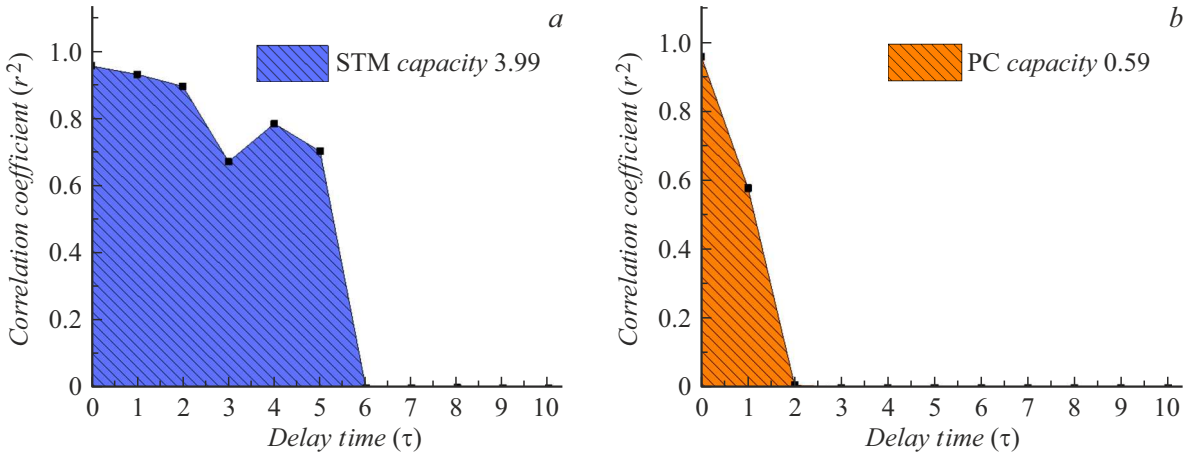

Figure 14. Results of the calculation of STMT (a) and PCT (b) for MARO on the SWDL of the basic design.

Results of calculation of the capacities of STMT and PCT of microminiature RCS on SWDL of various designs

№	Parameter	STMT capacity	Δ_{STMT}	PCT capacity	Δ_{PCT}	T/τ
1	—	3.99	0	0.59	0	8.59
2	$\Delta_g = 235$ nm	3.76	−0.23	0.54	−0.05	8.1
3	$\Delta_g = 435$ nm	1.4	−2.59	1.29	0.7	9.11
4	$w_g = 520$ nm	3.4	−0.59	0.67	0.08	9.37
5	$w_g = 255$ nm	5.02	1.03	0.6	0.01	8.44
6	$w = 440$ nm	2.82	−1.17	0.59	0	8.08
7	$w = 885$ nm	4.76	0.77	0.59	0	8.07
8	$l_s = 50\,\mu$m	2.76	−1.23	0.59	0	8.08
9	$l_s = 35\,\mu$m	4.14	0.15	0.55	−0.04	8.39
10	$\rho \to 0$	3.73	−0.26	0.71	0.12	8.42
11	$L = 50$ nm	4.6	0.61	0.41	−0.18	6.23
12	$L = 125$ nm	0.91	−3.08	1.27	0.68	9.01
13	$H = 222.82$ kA/m	2.53	−1.46	0.64	0.05	5.34

Conclusion

New knowledge was gained in this study about the possibility of microminiaturization of magnonic RCS through the use of ultrathin YIG films. Transmission characteristics of microminiature SWDL on ultrathin films of YIG were calculated for this purpose. The SWDL design uses compact coplanar antennas, which ensure an effective excitation and reception of spin waves, as well as isolation between antennas outside the operating frequency band. The impact of the parameters of coplanar antennas on the transmission characteristics of the SWDL was studied. The obtained dependences were used to calculate the amplitude-frequency characteristics of active ring resonators. The numerical simulation demonstrated that the use of nanometer-sized YIG films ensures the preservation of the delay time and the level of insertion losses with a waveguide structure length of only $20\,\mu$m, which is two orders of magnitude less than in the case of YIG films of micron thickness. The obtained characteristics of microminiature SWDL and active ring resonators were used to simulate transients in magnonic RCS at the final stage of the study where the gain control is used for information message input. The calculation of the STMT and PCT capacity was used to evaluate the performance of computing systems. It was shown that the characteristics of the proposed magnonic microreservoirs are not inferior to the characteristics of classical magnonic RCS on micron films. It should be noted that the use of microchips as a microwave amplifier and an electronic attenuator makes it possible to produce magnonic RCS with a hybrid design using thin-film technology for creating microminiature RCS.

Funding

This study at Saint Petersburg Electrotechnical University was supported by the Ministry of Science and Higher Education of the Russian Federation (project „State Assignment“, grant № FSEE-2020-0005).

Conflict of interest

The authors declare that they have no conflict of interest.

References

[1] D.P. Mandic, J.A. Chambers. *Recurrent Neural Networks for Prediction Learning Algorithms, Architectures and Stability*. (Wiley Online Library, 2001), DOI: 10.1002/047084535X

[2] G G. Tanaka, T. Yamane, J. B. Héroux, R. Nakane, N. Kanazawa, S. Takeda, H. Numata, D. Nakano, A. Hirose. Neural Netw., **115**, 100 (2019). DOI: 10.1016/j.neunet.2019.03.005

[3] G. Dion, S. Mejaouri, J. Sylvestre. J. App. Phys., **124**, 152132 (2018). DOI: 10.1063/1.5038038

[4] Y. Paquot, F. Duport, A. Smerieri, J. Dambre, B. Schrauwen, M. Haelterman, S. Massar. Sci. Rep., **2**, 282 (2012). DOI: 10.1038/srep00287

[5] Y.K. Chembo, D. Brunner, M. Jacquot, L. Larger. Rev. Mod. Phys., **91**, 035006 (2019). DOI: 10.1103/RevModPhys.91.035006

[6] Y. Bai, X. Xu, M. Tan, Y. Sun, Y. Li, J. Wu, R. Morandotti, A. Mitchell, K. Xu, D.J. Moss. Nanophotonics, **12**, 795 (2023). DOI: 10.1515/nanoph-2022-0485

[7] F.D.-L. Coarer, M. Sciamanna, A. Katumba, M. Freiberger, J. Dambre, P. Bienstman, D. Rontani. IEEE J. Sel Top. Quantum Electron., **24**, 7600108 (2018). DOI: 10.1109/JSTQE.2018.2836985

[8] Y. Yamazaki, K. Kinoshita. Adv. Sci., **11**, 2304804 (2023). DOI: 10.1002/advs.202304804

[9] Y. Zhong, J. Tang, X. Li, X. Liang, Z. Liu, Y. Li, Y. Xi, P. Yao, Z. Hao, B. Gao, H. Qian, H. Wu. Nat., Electron., **5**, 672 (2022). DOI: 10.1038/s41928-022-00838-3

[10] J. Grollier, D. Querlioz, K. Camsari, K. Everschor-Sitte, S. Fukami, M.D. Stiles. Nat. Electron., **3**, 360 (2020). DOI: 10.1038/s41928-019-0360-9

[11] J. Torrejon, M. Riou, F.A. Araujo, S. Tsunegi, G. Khalsa, D. Querlioz, P. Bortolotti, V. Cros, K. Yakushiji, A. Fukushima, H. Kubota, S. Yuasa, M.D. Stiles, J. Grollier. Nat., **547**, 428 (2017). DOI: 10.1038/nature23011

[12] K. Nakajima. Jpn. J. Appl. Phys., **59**, 060501 (2020). DOI: 10.35848/1347-4065/ab8d4f

[13] K. Nakajima.*Reservoir Computing* (Singapore: Springer, 2021), DOI: 10.1007/978-981-13-1687-6

[14] Z. Qi, L. Mi, H. Qian, W. Zheng, Y. Guo, Y. Chai. Adv. Funct. Mater., **33**, 2306149 (2023). DOI: 10.1002/adfm.202306149

[15] M. Yan, C. Huang, P. Bienstman, P. Tino, W. Lin, J. Sun. Nat. Commun., **15**, 2056 (2024). DOI: 10.1038/s41467-024-45187-1

[16] X. Liang, J. Tang, Y. Zhong, B. Gao, H. Qian, H. Wu. Nat. Electron. **7**, 193 (2024). DOI: 10.1038/s41928-024-01133-z

[17] H. Jaeger. *A tutorial on training recurrent neural networks, covering BPPT, RTRL, EKF and the „echo state network" approach* (2005)

[18] N. Bertschinger, T. Natschläger. Neural Comput., **16**, 1413 (2004). DOI: 10.1162/089976604323057443

[19] S. Watt, M.P. Kostylev. Phys. Rev. Appl., **13**, 034057 (2020). DOI: 10.1103/PhysRevApplied.13.034057.

[20] S. Watt, M.P. Kostylev, A.B. Ustinov. J. Appl. Phys., **129**, 044902 (2021). DOI: 10.1063/5.0033292

[21] S. Watt, M.P. Kostylev, A.B. Ustinov, B.A. Kalinikos. Phys. Rev. Appl., **15**, 064060 (2021). DOI: 10.1103/PhysRevApplied.15.064060

[22] A.B. Ustinov, R.V. Haponchyk, M.A. Kostylev. Appl. Phys. Lett., **124**, 4 (2024). DOI: 10.1063/5.0189542

[23] S. Watt, M. Kostylev. J. Appl. Phys., **135** (2), (2024). DOI: 10.1063/5.0184848

[24] C.B. Abbott, D.A. Bozhko. (2024). DOI: 10.48550/arXiv.2405.09542

[25] M. Wu. Solid State Phys., **62**, 163 (2010). DOI: 10.1016/B978-0-12-374293-3.00003-1

[26] Z. Wang, A. Hagerstrom, J.Q. Anderson, W. Tong, M. Wu, L.D. Carr, R. Eykholt, B.A. Kalinikos. Phys. Rev. Lett., **107**, 114102 (2011). DOI: 10.1103/PhysRevLett.107.114102

[27] A. Hagerstrom, M. Wu, R. Eykholt, B.A. Kalinikos. Phys. Rev. B, **83**, 104402 (2011). DOI: 10.1103/PhysRevB.83.104402

[28] A.B. Ustinov, A.V. Kondrashov, A.A. Nikitin, B.A. Kalinikos. Appl. Phys. Lett., **104**, 234101 (2014). DOI: 10.1063/1.4881889

[29] P.A.P. Janantha, B. Kalinikos, M. Wu. Phys. Rev. B, **95**, 064422 (2017). DOI: 10.1103/PhysRevB.95.064422

[30] A.S. Bir, S.V. Grishin, O.I. Moskalenko, A.N. Pavlov, M.O. Zhuravlev, D.O. Ruiz. Phys. Rev. Lett., **125**, 083903 (2020). DOI: 10.1103/PhysRevLett.125.083903

[31] Y. Xiong, Z. Zhang, Y. Li, M. Hammami, J. Sklenar, L. Alahmed, P. Li, T. Sebastian, H. Qu, A. Hoffmann, V. Novosad, W. Zhang. Rev. Sci., **91**, 125105 (2020). DOI: 10.1063/5.0023715

[32] S.V. Grishin, O.I. Moskalenko, A.N. Pavlov, D.V. Romanenko, A.V. Sadovnikov, Y.P. Sharaevskii, I.V. Sysoev, T.M. Medvedeva, E.P. Seleznev, S.A. Nikitov. Phys. Rev. Appl., **16**, 054029 (2021). DOI: 10.1103/PhysRevApplied.16.054029

[33] A.B. Ustinov, A.V. Kondrashov, I. Tatsenko, A.A. Nikitin, M.P. Kostylev. Phys. Rev. B, **104**, L140410 (2021). DOI: 10.1103/PhysRevB.104.L140410

[34] J. Anderson, P.A. Praveen Janantha, D.A. Alcala, M. Wu, L.D. Carr. New J. Phys., **24**, 033018 (2022). DOI: 10.1088/1367-2630/ac47cb

[35] V.V. Vitko, A.A. Nikitin, R.V. Haponchyk, A.A. Stashkevich, M.P. Kostylev, A.B. Ustinov. Eur. Phys. J., **137**, 1010 (2022). DOI: 10.1140/epjp/s13360-022-03213-5

[36] A. Khitun, M. Balinskiy. Sci. Rep., **12**, 9482 (2022). DOI: 10.1038/s41598-022-13614-2

[37] M. Balynsky, Y. Khivintsev, A. Kozhevnikov, Y. Nikulin, V. Sakharov, Y. Filimonov, A. Khitun. J. Appl. Phys., **133**, 023904 (2023). DOI: 10.1063/5.0130423

[38] A.V. Chumak, P. Kabos, M. Wu, C. Abert, C. Adelmann, A.O. Adeyeye, J. Akerman, F.G. Aliev, A. Anane, A. Awad, C.H. Back, A. Barman, G.E.W. Bauer, M. Becherer, E.N. Beginin, V.A.S.V. Bittencourt, Y.M. Blanter, P. Bortolotti, I. Boventer, D.A. Bozhko, S.A. Bunyaev, J.J. Carmiggelt, R.R. Cheenikundil, F. Ciubotaru, S. Cotofana, G. Csaba, O.V. Dobrovolskiy, C. Dubs, M. Elyasi, K.G. Fripp, H. Fulara, I.A. Golovchanskiy, C. Gonzalez-Ballestero, P. Graczyk, D. Grundler, P. Gruszecki, G. Gubbiotti, K. Guslienko, A. Haldar, S. Hamdioui, R. Hertel, B. Hillebrands, T. Hioki, A. Houshang, C.-M. Hu, H. Huebl, M. Huth, E. Iacocca, M.B. Jungfleisch, G.N. Kakazei, A. Khitun, R. Khymyn, T. Kikkawa, M. Klaui, O. Klein, J.W. Klos, S. Knauer, S. Koraltan, M. Kostylev, M. Krawczyk, I.N. Krivorotov, V.V. Kruglyak, D. Lachance-Quirion, S. Ladak, R. Lebrun, Y. Li, M. Lindner, R. Macedo, S. Mayr, G.A. Melkov, S. Mieszczak, Y. Nakamura, H.T. Nembach, A.A. Nikitin, S.A. Nikitov, V. Novosad, J.A. Otalora, Y. Otani, A. Papp, B. Pigeau, P. Pirro, W. Porod, F. Porrati, H. Qin, B. Rana, T. Reimann, F. Riente, O. Romero-Isart, A. Ross,

A.V. Sadovnikov, A.R. Safin, E. Saitoh, G. Schmidt, H. Schultheiss, K. Schultheiss, A.A. Serga, S. Sharma, J.M. Shaw, D. Suess, O. Surzhenko, K. Szulc, T. Taniguchi, M. Urbanek, K. Usami, A.B. Ustinov, T. van der Sar, S. van Dijken, V.I. Vasyuchka, R. Verba, S.V. Kusminskiy, Q. Wang, M. Weides, M. Weiler, S. Wintz, S.P. Wolski, X. Zhang. IEEE Trans. Magn., **58** (6), 1 (2022). DOI: 10.1109/TMAG.2022.3149664

[39] S. Watt, M. Kostylev. Phys. Rev. Appl., **19** (6), 064029 (2023). DOI: 10.1103/PhysRevApplied.19.064029

[40] N. Beaulieu, N. Kervarec, N. Thiery, O. Klein, V. Naletov, H. Hurdequint, G. Loubens, J. B. Youssef, N. Vukadinovic. IEEE Magn. Lett., **9**, 1 (2018). DOI: 10.1109/LMAG.2018.2868700

[41] C. Dubs. Phys. Rev. Mater., **4**, 024416 (2020). DOI: 10.1103/PhysRevMaterials.4.024416

[42] A. K. Ganguly, D.C. Webb. IEEE Trans. Microw. Theory Tech., **2** (12), 998 (1975). DOI: 10.1109/TMTT.1975.1128733

[43] G.A. Vugalter, B.N. Gusaev, A.G. Gurevich, O.A. Chivileva. ZhTF, **56** (1), 149 (1986) (in Russian).

[44] V.F. Dmitriev, B.A. Kalinikos. Sov. Phys. J., **31** (11), 875 (1988). DOI: 10.1007/BF00893541

[45] W.S. Ishak. Proc. IEEE, **76** (2), 171 (1988). DOI: 10.1109/5.4393

[46] G.A. Vugalter, I.A. Gilinsky. Izv. vuzov. Radiofizika, **32**(10), 1187 (1989) (in Russian).

[47] V.F. Dmitriev. Radiotekhnika i elektronika, **35**(9), 1821 (1990) (in Russian).

[48] V. Vlaminck, M. Bailleul. Science, **322** (5900), 410 (2008). DOI: 10.1126/science.1162843

[49] C.S. Chang, M. Kostylev, E. Ivanov, J. Ding, A.O. Adeyeye. Appl. Phys. Lett., **104** (3), 032408 (2014). DOI: 10.1063/1.4863078

[50] C. Weiss, M. Grassi, Y. Roussigne, A. Stashkevich, T. Schefer, J. Robert, M. Bailleul, M. Kostylev. J. Magn. Magn. Mater., **565**, 170003 (2023). DOI: 10.1016/j.jmmm.2022.170103

[51] C. Weiss, M. Grassi, Y. Roussigne, A. Stashkevich, T. Schefer, J. Robert, M. Bailleul, M. Kostylev. Magn. Magn. Mater., **565**, 170002 (2023). DOI: 10.1016/j.jmmm.2022.170002

[52] A.A. Nikitin, I.Y. Tatsenko, M.P. Kostylev, A.B. Ustinov. J. Appl. Phys., **135**, 123906 (2024). DOI: 10.1063/5.0200249

[53] A.A. Nikitin, A.A. Nikitiv, A.B. Ustinov, S. Watt, M.P. Kostylev. J. Appl. Phys., **131** (11), 113903 (2022). DOI: 10.1063/5.0081142

[54] A.V. Kondrashov, A.A. Nikitin, A.A. Nikitin, M.P. Kostylev, A.B. Ustinov. J. Magn. Magn. Mater., **563**, 169968 (2022). DOI: 10.1016/j.jmmm.2022.169968

[55] A.A. Nikitin, V.V. Vitko, M.A. Cherkasskii, A.B. Ustinov, B.A. Kalinikos. Res. Phys., **18**, 103279 (2020). DOI: 10.1016/j.rinp.2020.103279

[56] V.E. Demidov, B.A. Kalinikos, N.G. Kovshikov, P. Edenhofer. Electron. Lett., **35** (21), 1856 (1999). DOI: 10.1049/el:19991140

[57] A.A. Nikitin, A.B. Ustinov, A.A. Semenov, B.A. Kalinikos. ZhTF, **82** (7), 98 (2012) (in Russian). DOI: 10.1134/S106378421207016X

[58] M.M. Scott, C.E. Patton, M.P. Kostylev, B.A. Kalinikos. J. Appl. Phys., **95**, 6294 (2004). DOI: 10.1063/1.1699503

[59] A.B. Ustinov, B.A. Kalinikos. Appl. Phys. Lett., **89**, 172511 (2006). DOI: 10.1063/1.2362576

[60] A.V. Kondrashov, M. Kostylev, A.B. Ustinov. J. Magn. Magn. Mater., **591**, 171685 (2024). DOI: 10.1016/j.jmmm.2023.171685

Translated by A.Akhtyamov